

Connections between resonant inelastic x-ray scattering and complementary x-ray spectroscopies: Probing excitons at the Al K and L_1 edges of α -Al₂O₃

M. Laura Urquiza ^{1,2}, Matteo Gatti,^{1,2,3} and Francesco Sottile ^{1,2}

¹*LSI, CNRS, CEA/DRF/IRAMIS, École Polytechnique, Institut Polytechnique de Paris, F-91120 Palaiseau, France*

²*European Theoretical Spectroscopy Facility (ETSF)*

³*Synchrotron SOLEIL, L'Orme des Merisiers, Saint-Aubin, BP 48, F-91192 Gif-sur-Yvette, France*



(Received 15 December 2023; revised 22 February 2024; accepted 23 February 2024; published 28 March 2024)

We present an *ab initio* study of neutral core and valence electronic excitations in α -Al₂O₃ by solving the Bethe-Salpeter equation (BSE) of many-body perturbation theory within an all-electron framework. Calculated spectra at the Al K and L_1 edges are in remarkable agreement with available experiments from x-ray absorption (XAS) and x-ray Raman spectroscopy once excitonic effects are taken into account. The combination of the BSE spectra for the two techniques confirms the dipole-forbidden nature of the exciton prepeak as suggested by recent calculations based on density-functional theory. Moreover, we make predictions for resonant inelastic x-ray scattering (RIXS) spectra at K and L_1 edges, which strikingly fully overlap also beyond an independent-particle picture. The RIXS calculations reveal two distinct regimes as a function of incoming photon energy. Below and at the XAS threshold, we observe Raman-like features, characterized by strong excitonic effects, which we directly compare to peaks in the loss function. Above the XAS threshold, instead, fluorescence features become predominant: RIXS spectra can be well described and analyzed within an independent-particle approximation showing similarity with the x-ray emission spectrum.

DOI: [10.1103/PhysRevB.109.115157](https://doi.org/10.1103/PhysRevB.109.115157)

I. INTRODUCTION

The past decades have witnessed huge progress in both the experimental resolution [1–3] and computational accuracy [4–6] of x-ray spectroscopies that probe core levels in materials. Core-level spectroscopies [7] have thus become a key tool for the study of a vast number of materials properties, which is evidenced by the surge of interest in their applications across chemistry, physics, biology, and materials science [8].

The fundamental processes of photon absorption, emission, and scattering give rise to prominent spectroscopies that measure neutral electronic excitations in materials [9]. X-ray absorption (XAS), also referred as x-ray absorption near-edge spectroscopy, is determined by electronic transitions from core levels to unoccupied states, while x-ray emission (XES) stems from the decay of valence electrons to fill a core hole, providing complementary information on occupied states. Finally, resonant inelastic x-ray scattering [10] (RIXS) results from the coherent combination of x-ray absorption and emission. In RIXS, the energy of an incoming photon is tuned to resonate with a specific core level, and the subsequent relaxation of a valence electron to fill the core hole is accompanied by the emission of a photon of lower energy. As a result, RIXS probes low-energy excitations of the various degrees of freedom (i.e., charge, spin, lattice) of materials [2,11]. If, instead, the incident photon energy is much higher than the typical binding energies of core levels, one has the nonresonant inelastic x-ray scattering [10] (NRIXS), also called x-ray Raman scattering (XRS) when used to measure core-level properties.

These x-ray spectroscopies share attractive properties. The large penetration depth of photons, especially in the hard x-ray regime, allows better bulk sensitivity than for spectroscopies that make use of electrons, such as photoelectron spectroscopy. Moreover, the use of the distinctive atomic transitions (i.e., the absorption edges) of the different kinds of atoms ensures chemical sensitivity, providing element- and orbital-specific information of the local chemical environments in complex materials. In particular, the selection rules of the photoexcitation make it convenient to identify the character of the electronic excitations. Within an independent-particle picture, XES and XAS spectra can be simply related, respectively, to the occupied and unoccupied projected density of states (PDOS) of the absorbing atom with the angular momentum component that fulfils the selection rules. Similarly, RIXS spectra can be associated to the projected joint density of states (JDOS).

However, electron-electron interactions can dramatically alter this independent-particle picture. In particular, according to the semiempirical final-state rule [12,13], one has to deal with the strong perturbing potential due the presence of a core hole in the final state. Indeed, the electron-hole attraction gives rise to core excitons in XAS and XRS, and to both core and valence excitons in RIXS. Excitons manifest as strong enhancements of the spectral weight at the onsets and are often even the main feature in the spectra.

To take into account the effects of the electronic interactions, a variety of methods have been developed at different levels of approximation, ranging from the real-space multiple-scattering formalism [14–16] to cluster models [17–19] and many-body perturbation theory [20–29] (MBPT). Within

the context of MBPT, the first-principles solution of Bethe-Salpeter equation [30,31] (BSE) is nowadays the state-of-the-art approach to deal with excitonic effects for both core and valence excitations [32,33]. The BSE within an all-electron framework [34] will therefore be adopted in the present paper.

The aims of the present paper are to conduct an in-depth analysis of RIXS spectra, while accounting for coherence and excitonic effects throughout the entire process, and to establish direct connections with the complementary spectroscopy techniques that also measure neutral excitations in materials, such as XAS, XRS, and XES. Our paper is focused on α -Al₂O₃, which is a prototypical wide-band-gap insulator with a broad range of applications, including catalysis, ceramics, and electronics [35,36]. Since the BSE has consistently demonstrated its accuracy in describing similar experiments, our conclusions can be reliably extended to other wide-band-gap materials.

We have calculated XAS and XRS spectra at the Al *K* edge reproducing very well the available experimental spectra [37,38] when strong excitonic effects, which determine the main peak in the spectra, are properly taken into account. Consistently with results from literature, we find that an excitonic prepeak is also present in the XRS spectrum at large momentum transfer. This prepeak is not visible in the calculated XAS spectrum because dipole forbidden, while it is enabled in the experiments by the coupling with atomic vibrations. Moreover, we demonstrate that both XAS and RIXS spectra at the Al *L*₁ edge are the same as the corresponding spectra at the Al *K* edge, which suggests that *L*₁ edges could be a valuable alternative in the soft x-ray regime to *K* edges that require hard x rays. The analysis of RIXS spectra shows that excitonic effects are mostly visible for excitation energies smaller than (or similar to) the absorption edges and how, for higher excitation energies, the RIXS spectra tend to XES spectra where excitonic effects are less relevant.

The paper is organized as follows. In Sec. II, we briefly present the basic theoretical concepts for the calculation of the spectra, together with a summary of the computational details. In Sec. III A, we discuss the calculated XAS and XRS spectra at the Al *K* edge. RIXS spectra for *K* and *L*₁ edges are then compared and analyzed in Sec. III B. Finally, in Sec. IV, we summarize the main conclusions and give an outlook of the present paper.

II. THEORETICAL FRAMEWORK AND COMPUTATIONAL DETAILS

A. The Bethe-Salpeter equation for excitation spectra

The BSE is an in-principle exact equation for the electron-hole correlation function, which is directly linked to the various neutral electronic excitation spectra [32,33]. Within the *GW* approximation [39] and using a statically screened Coulomb interaction *W*, the BSE can be expressed as an eigenvalue problem for the two-particle excitonic Hamiltonian [40]: $\bar{H}_{\text{exc}}\bar{A}_\lambda = \bar{A}_\lambda\bar{E}_\lambda$.

The matrix elements of the excitonic Hamiltonian can be written in the basis of electron-hole transitions *t* between Bloch orbitals [41] $n_1\mathbf{k}_1 \rightarrow n_2\mathbf{k}_2$, which in the

ab initio framework are usually calculated within the Kohn-Sham scheme [42] of density-functional theory (DFT).

In this basis, the matrix elements read

$$\langle t | \bar{H}_{\text{exc}} | t' \rangle = E_t \delta_{tt'} + \langle t | \bar{v}_c - W | t' \rangle. \quad (1)$$

Here E_t is the independent-particle excitation energy calculated in the *GW* approximation. \bar{v}_c is the Coulomb interaction without its long-range, macroscopic, component:

$$\bar{v}_c(\mathbf{q} + \mathbf{G}) = \begin{cases} 4\pi/|\mathbf{q} + \mathbf{G}|^2 & \text{for } \mathbf{G} \neq 0 \\ 0 & \text{for } \mathbf{G} = 0, \end{cases} \quad (2)$$

where \mathbf{G} is a reciprocal-lattice vector and \mathbf{q} is a wave vector in the first Brillouin zone. The modified Coulomb interaction \bar{v}_c enters the excitonic Hamiltonian as an exchange electron-hole repulsion and is responsible for crystal local field effect [43,44]. The screened Coulomb interaction *W* is calculated in the random-phase approximation (RPA). It plays the role of the direct electron-hole attraction and is responsible for excitonic effects.

In the Tamm-Dancoff approximation [45] (which will be assumed henceforth), one considers only resonant transitions between occupied states n_1 and empty states n_2 . For XAS spectra, n_1 is a core level μ , while for optical spectra n_1 is a valence band v . In both cases, the absorption spectra, which are described by the imaginary part of the macroscopic dielectric function $\text{Im}\epsilon_M(\omega)$ in the long wavelength limit $\mathbf{q} \rightarrow 0$, are obtained in terms of the excitonic eigenvectors \bar{A}_λ and eigenvalues \bar{E}_λ as [40]

$$\text{Im}\epsilon_M(\omega) = \lim_{\mathbf{q} \rightarrow 0} \frac{8\pi^2}{\Omega q^2} \sum_\lambda \left| \sum_t \bar{A}_\lambda^t \tilde{\rho}_t(\mathbf{q}) \right|^2 \delta(\omega - \bar{E}_\lambda), \quad (3)$$

where Ω is the volume of the system and the oscillator strengths $\tilde{\rho}_t(\mathbf{q})$ are defined as

$$\tilde{\rho}_t(\mathbf{q}) = \langle n_1 \mathbf{k} - \mathbf{q} | e^{-i\mathbf{q}\cdot\mathbf{r}} | n_2 \mathbf{k} \rangle. \quad (4)$$

By setting the direct electron-hole interaction *W* to 0 in the excitonic Hamiltonian (1), one finds the absorption spectra within RPA. Moreover, by switching off both electron-hole interactions \bar{v}_c and *W*, the independent-particle approximation (IPA) is retrieved and the absorption spectrum becomes

$$\text{Im}\epsilon_M(\omega) = \lim_{\mathbf{q} \rightarrow 0} \frac{8\pi^2}{\Omega q^2} \left| \sum_t \tilde{\rho}_t(\mathbf{q}) \right|^2 \delta(\omega - E_t). \quad (5)$$

The direct comparison between Eqs. (3) and (5) shows that the electron-hole interactions affect the spectra in two ways: by modifying the peak positions, through a change of excitation energies from the interband transition energies E_t to the excitonic energies \bar{E}_λ , and by altering the peak intensities, through the mixing of the independent-particle transitions that are weighted by the excitonic coefficients \bar{A}_λ .

In XES spectra, the transitions *t* take place between occupied valence states v and empty core levels μ . In this case, there are no electron-hole interactions since both initial and final states contain one hole, but no excited electron. Therefore, XES spectra are usually calculated in the independent-particle

picture [46]. In the dipole limit, one has

$$I^{\text{XES}}(\omega) \propto \lim_{\mathbf{q} \rightarrow 0} \frac{8\pi^2}{\Omega q^2} \left| \sum_t \tilde{\rho}_t(\mathbf{q}) \right|^2 \delta(\omega - E_t). \quad (6)$$

In this approximation, one neglects the effect of the core hole on valence states [47].

By further assuming that the oscillator strengths in Eqs. (5) and (6) fulfill the dipole selection rule, but are transition-independent constants, the spectra would be equivalent to the PDOS for empty states in XAS and the PDOS for occupied states for XES.

If, at variance with Eq. (1), the excitonic Hamiltonian H_{exc} includes the full Coulomb interaction v_c ,

$$\langle t | H_{\text{exc}} | t' \rangle = E_t \delta_{tt'} + \langle t | v_c - W | t' \rangle, \quad (7)$$

one obtains the loss function, i.e., the inverse macroscopic dielectric function [48]

$$-\text{Im}\epsilon_M^{-1}(\mathbf{q}, \omega) = \frac{8\pi^2}{\Omega q^2} \sum_\lambda \left| \sum_t A_\lambda^t \tilde{\rho}_t(\mathbf{q}) \right|^2 \delta(\omega - E_\lambda) \quad (8)$$

in terms of the excitonic eigenvectors and eigenvalues: $H_{\text{exc}} A_\lambda = E_\lambda A_\lambda$. By comparing the two excitonic Hamiltonians Eqs. (1) and (7), we understand that the long-range component $\mathbf{G} = 0$ of the Coulomb interaction v_c gives rise to the difference between the macroscopic dielectric function ϵ_M in the $\mathbf{q} \rightarrow 0$ limit, see Eq. (3), and its inverse ϵ_M^{-1} , see Eq. (8). When the electronic states are localized, such as for core levels, the long-range component $\mathbf{G} = 0$ of the Coulomb interaction v_c becomes ineffective in the excitonic Hamiltonian (8), and therefore the two spectra (3) and (8) coincide [40,49,50].

NRIXS usually investigates electron-hole transitions t from valence bands v to conduction bands c , while XRS focuses on transitions from core levels μ to conduction bands c . In both cases, the excitation spectra are described by the dynamic structure factor [10], which is proportional to the loss function (8). A big advantage of scattering spectroscopies with respect to absorption is the possibility to probe electronic excitations as a function of the momentum transfer \mathbf{q} , going well beyond the dipole limit $\mathbf{q} \rightarrow 0$.

In the case of RIXS [51], the excitonic Hamiltonian (7) has to be solved twice. In the first BSE, one deals with a core exciton Hamiltonian $H_{\text{exc}} A_{\lambda_\mu} = E_{\lambda_\mu} A_{\lambda_\mu}$, where the electron-hole transitions t_μ are from core levels μ to conduction bands c . In the second BSE, one has a valence exciton Hamiltonian, $H_{\text{exc}} A_{\lambda_o} = E_{\lambda_o} A_{\lambda_o}$, where the transitions t_o are from valence bands v to conduction bands c . Here we consider only vertical interband excitations at the same \mathbf{k} point, i.e., we calculate RIXS spectra in the long-wavelength limit.

RIXS spectra can then be obtained from the two sets of excitonic eigenvalues and eigenvectors as [27,28]

$$I^{\text{RIXS}}(\omega_1, \omega) \propto \sum_{\lambda_o} \left| \sum_{\lambda_\mu} \frac{t_{\lambda_\mu}^{(1)} t_{\lambda_o, \lambda_\mu}^{(2)}}{\omega_1 - E_{\lambda_\mu} + i\Gamma/2} \right|^2 \delta(\omega - E_{\lambda_o}). \quad (9)$$

Here the energy loss ω is equal to the difference between the incident photon energy ω_1 and the emitted photon energy ω_2 :

$\omega = \omega_1 - \omega_2$, $1/\Gamma$ is the lifetime of the core hole and the oscillator strengths are

$$t_{\lambda_\mu}^{(1)} = \sum_{\mu\mathbf{c}\mathbf{k}} A_{\lambda_\mu}^{\mu\mathbf{c}\mathbf{k}} \langle \mathbf{c}\mathbf{k} | \mathbf{e}_1 \cdot \mathbf{p} | \mu\mathbf{k} \rangle, \quad (10)$$

$$t_{\lambda_o, \lambda_\mu}^{(2)} = \sum_{v\mathbf{c}\mathbf{k}} \sum_{\mu} A_{\lambda_o}^{v\mathbf{c}\mathbf{k}} \langle \mu\mathbf{k} | \mathbf{e}_2^* \cdot \mathbf{p} | v\mathbf{k} \rangle \left[A_{\lambda_\mu}^{\mu\mathbf{c}\mathbf{k}} \right]^*, \quad (11)$$

with \mathbf{p} the momentum operator and \mathbf{e}_1 and \mathbf{e}_2 the light polarization unity vectors [52].

While the possible peak positions in the scattering spectra from Eqs. (8) and (9) are the same, their intensities can be very different. For example, in contrast to NRIXS, RIXS spectra even in the dipole limit can display dipole-forbidden excitations, such as d - d transitions [2,11,53], since they stem from a different two-step process. In general, RIXS spectra strongly depend on the excitation energies ω_1 in the denominators of Eq. (9). For fixed excitation energy ω_1 , RIXS spectra are usually plotted and analyzed as a function of the energy loss ω [i.e., as $I^{\text{RIXS}}(\omega_1, \omega = \omega_1 - \omega_2)$] or of the emission energy ω_2 [i.e., as $I^{\text{RIXS}}(\omega_1, \omega_2)$].

In the IPA, the RIXS spectrum (9) becomes

$$I^{\text{RIXS}}(\omega_1, \omega) \propto \sum_{c\nu\mathbf{k}} \left| \sum_{\mu} \frac{\langle \mathbf{c}\mathbf{k} | \mathbf{e}_1 \cdot \mathbf{p} | \mu\mathbf{k} \rangle \langle \mu\mathbf{k} | \mathbf{e}_2^* \cdot \mathbf{p} | \nu\mathbf{k} \rangle}{\omega_1 - (\varepsilon_{c\mathbf{k}} - \varepsilon_{\mu\mathbf{k}}) + i\Gamma/2} \right|^2 \times \delta(\omega - (\varepsilon_{c\mathbf{k}} - \varepsilon_{\nu\mathbf{k}})), \quad (12)$$

which is given by a combination of vertical transitions (i.e., at the same \mathbf{k} point) between core levels of energies $\varepsilon_{\mu\mathbf{k}}$, valence bands $\varepsilon_{\nu\mathbf{k}}$, and conduction bands $\varepsilon_{c\mathbf{k}}$. If the peak intensities are further assumed to be constant in Eq. (12), the RIXS signal becomes proportional to the JDOS (projected on the angular component selected by the excitation-disexcitation process). When electron-hole interactions are weak, one may therefore relate RIXS to band-structure properties [11,21,54–58]. On the contrary, excitonic effects also in the RIXS spectra mix the various interband transitions, blurring the picture based on the single-particle band structure.

B. Computational details

The computational strategy of the present paper follows the one that we have already successfully employed for α -Al₂O₃ in Ref. [59]. We have adopted the experimental lattice parameter [60] $a_0 = 5.128$ Å and angle $\alpha = 55.287$ in the rhombohedral primitive cell. Calculations have been performed using the full-potential all-electron (AE) approach, as implemented in the EXCITING code [34,61]. The Kohn-Sham ground-state wave functions have been calculated within the local density approximation [42] (LDA) of DFT. The Brillouin zone has been sampled with a $6 \times 6 \times 6$ \mathbf{k} -grid, using plane wave (PW) expansion with a cutoff energy of 12 Hartree. The AE approach includes muffin-tin spheres with radii of 2 bohr and 1.45 bohr for aluminum and oxygen, respectively.

BSE calculations are performed on a $8 \times 8 \times 8$ \mathbf{k} -grid shifted by (0.05, 0.15, 0.25). In XAS and RIXS simulations, BSE matrix elements are calculated with a cutoff $|\mathbf{G} + \mathbf{q}|_{\text{max}} = 4 a_0^{-1}$, maintaining a PW cutoff of 7 Hartree for the wave functions. XRS calculations are performed with a PW cutoff of 10 Hartree and $|\mathbf{G} + \mathbf{q}|_{\text{max}} = 7 a_0^{-1}$.

To obtain the RPA screening of W , we used the same parameters as in the BSE, including 100 conduction bands. The BSE Hamiltonian was constructed considering 12 (4) occupied states and 20 (60) unoccupied states for the optical (L_1 and K edge) spectrum. To take into account GW corrections [62], the LDA band gap has been opened by a rigid scissor correction of 2.64 eV. Excitation spectra at the Al L_1 and K edges have been aligned with the experimental spectra, applying a downshift of the corresponding LDA core level energies of 17.18 eV and 61.9 eV, respectively. For the XRS spectrum, the downshift is 61.2 eV. XAS and XRS spectra for the Al K edge have been convoluted with a Lorentzian broadening of 0.7 eV to match the experimental broadening, bigger than the inverse core-hole lifetime of 0.42 eV [63,64].

The K and L_1 RIXS spectra have been calculated with the BRIXS code [27,65], considering the first (lowest-energy) 17 000 and 80 000 BSE eigenvectors and eigenvalues for the core and valence excitations, respectively, which gives a converged RIXS spectrum for an energy loss window of 20 eV.

For a better comparison between RIXS spectra at Al K and L_1 edges we have used the same core-hole inverse lifetime Γ of 0.2 eV. The RIXS and XES spectra have been plotted using a broadening of 0.1 eV.

III. RESULTS AND DISCUSSION

α - Al_2O_3 is made of alternate layers of Al and O atoms that are stacked along the z axis of our Cartesian reference frame. The nature of the chemical bond is largely ionic: the valence bands have mostly O $2p$ character, while the bottom conduction band is mainly due to Al $3s$. The wide band gap [66,67] of ~ 9.6 eV concurs with the low dielectric constant [68,69] of ~ 3 to give rise to strong excitonic effects for both valence and core excitations [59,62].

Since the final state of XAS is the intermediate state of RIXS, its analysis is propaedeutic to understand RIXS spectra. Therefore, in Sec. III A we will first analyze XAS and XRS spectra before moving to the study of RIXS spectra in Sec. III B.

A. XAS and XRS at Al K

Figure 1 compares the absorption spectra at the Al K edge calculated within the IPA, the RPA, and the BSE with the measured and simulated XAS from Ref. [37]. The top and bottom panels display the spectra for two polarization directions: parallel (xy) and perpendicular (z) to the Al_2O_3 layers, respectively. The polarized XAS experiment has been done at $T=300$ K on a single crystal: the two measured spectra distinguish the two orientations.

Like for the optical spectra and the shallower core edges [59], the two Al K edge XAS spectra [37] display only a small anisotropy, which is very well captured by the BSE calculations. The IPA and RPA curves are on top of each other, meaning that the contribution of crystal local fields is negligible. This result may seem surprising since Al $1s$ electrons are localized, giving rise to an inhomogeneous charge response that could be responsible for strong local fields [40]. However, $1s$ electrons are also not highly polarizable, which implies

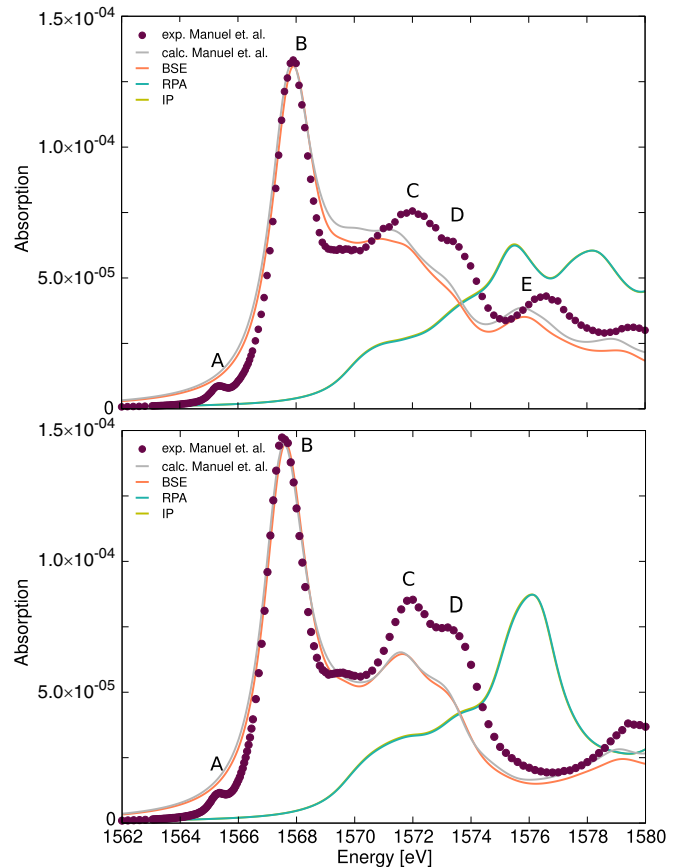


FIG. 1. Al K edge absorption spectra calculated within the IPA, RPA and BSE for two polarization directions: (top panel) parallel (xy) and (bottom panel) perpendicular (z) to the α - Al_2O_3 layers. The IPA and RPA spectra are on top of each other, highlighting the negligible contribution of local fields. For both polarizations the calculated spectra are compared to experimental and simulated XAS spectra from Manuel *et al.* [37], which have been normalized to match the maximum of the BSE intensity. The experiment has been done at $T = 300$ K and the simulation has been carried out in a DFT core-hole approach (where the coupling with atomic vibrations is excluded).

that the induced charge is so small that local field effects are negligible. On the contrary, taking into account excitonic effects in the BSE spectra is crucial to reproduce the main features of the experiments, notably the most prominent peak (B) and the secondary peaks (C) and (D). The ratio between the features (B) and (C) is an important indicator for aluminium coordination [70,71] used, in particular, to distinguish the tetrahedral AlO_4 from the octahedral AlO_6 of α - Al_2O_3 .

In the experimental spectra, there is also a prepeak (A) at ~ 1566 eV that is not present in the calculated spectra. In the BSE calculation, we actually find an excitonic eigenvalue \bar{E}_λ at the same energy. However, its oscillator strength is negligibly small, i.e., it is a *dark* exciton. Indeed, it corresponds to electron-hole transitions from the $1s$ core level to the bottom of the conduction band around the Γ point with mostly $3s$ character, which therefore are dipole forbidden. This prepeak (A) has been extensively studied both theoretically and experimentally [37,72–79]. The current interpretation is that atomic

vibrations enhance the Al sp hybridization at the bottom of the conduction band, by deviating the Al atoms from their centrosymmetric positions and thus enabling Al $1s \rightarrow 3p$ atomiclike transitions in the measured XAS spectra. Between the prepeak (A) and the main peak (B), we also identify additional excitons that have low oscillator strengths but are not completely dark. They correspond to transitions from $1s$ states to the first conduction band for \mathbf{k} points between Γ and T, characterized by nonzero Al sp hybridisation.

The binding energy of the lowest energy dark exciton is 1.69 eV, while the three main exciton peaks (B), (C), and (D) are within the continuum of electron-hole transitions of the IPA spectrum.

Finally, we find remarkable agreement, for both polarizations, between the BSE spectra and the results of the calculations (where the coupling with atomic vibrations is excluded) of Ref. [37] that has used a core-hole approach within DFT. The BSE takes explicitly into account the interaction between the core hole and the electron excited in the conduction band through Eq. (1). The result of the strong electron-hole attraction is the tight localization of the two-correlated-particle excitonic state around the core hole at the Al atom [59], namely, a Frenkel-like exciton with atomic character. The core-hole DFT approach instead adopts a supercell scheme with a pseudopotential with a core hole localized on an Al atom. The core-hole-electron interaction is implicitly taken into account by a self-consistent Kohn-Sham calculation in presence of the core hole. In the present case, these two very different approaches give the same result. It should also be noted that in Ref. [37] it has been shown how the treatment of the coupling with atomic vibration is crucial to improve the agreement with experiments, notably to explain the origin of prepeak (A) in XAS. On the side of the BSE, it is in principle analogously possible to describe the exciton-phonon coupling [80–83]. This is beyond the scope of the present paper, but the results here discussed call for further detailed comparisons between different methods dealing with the coupling with atomic vibrations.

To corroborate the interpretation that prepeak (A) in the XAS is associated to a dipole-forbidden exciton, we also calculate the XRS spectra from the solution of the BSE at the same Al K edge.

In the dipole limit $\mathbf{q} \rightarrow 0$, for localized electrons such as core levels, the loss function [measured by XRS, see Eq. (8)] tends to the absorption spectrum [measured by XAS, see Eq. (3)]:

$$-\text{Im}\epsilon_M^{-1}(\omega) = \frac{\text{Im}\epsilon_M(\omega)}{[\text{Re}\epsilon_M(\omega)]^2 + [\text{Im}\epsilon_M(\omega)]^2} \rightarrow \text{Im}\epsilon_M(\omega). \quad (13)$$

Mathematically, this results from $\text{Im}\epsilon_M(\omega) \ll \text{Re}\epsilon_M(\omega) \rightarrow 1$. In this situation, the absorption spectrum and the loss function yield the same information. As the magnitude of the momentum transfer \mathbf{q} increases, instead, XRS probes nondipolar transitions, potentially leading to the emergence of features not visible in the XAS spectra.

The BSE loss functions calculated for different momentum transfers \mathbf{q} along the x and z Cartesian directions are shown in Fig. 2 and compared to the experimental XRS spectrum [38]

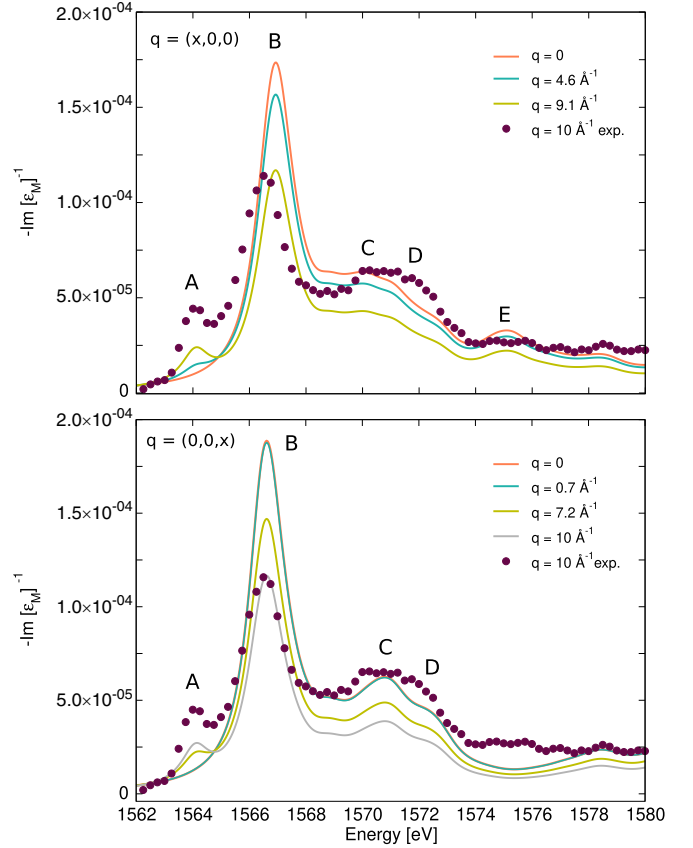


FIG. 2. Loss function calculated within the BSE for momentum transfers \mathbf{q} along the x (top) and z (bottom) Cartesian directions, with a broadening of 0.7 eV. The experimental XRS spectrum from Ref. [38] was measured for momentum transfer $|\mathbf{q}| = 10 \text{ \AA}^{-1}$. Here, it has been scaled to match the maximum intensity of the calculated spectrum at $|\mathbf{q}| = 10 \text{ \AA}^{-1}$. We note that the peak positions of the XRS spectrum [38] have a redshift of ~ 0.7 eV with respect to the XAS spectra in Fig. 1.

for $q = 10 \text{ \AA}^{-1}$. The measurement was done on a powder sample, therefore its momentum direction dependence could not be resolved. Also in this case the agreement between the BSE spectrum and experiment is noteworthy and could be further improved by taking into account the coupling with atomic vibrations [38].

In the dipole limit $\mathbf{q} \rightarrow 0$, the loss functions match the corresponding absorption spectra in Fig. 1, as expected from the previous discussion. The loss function remains the same, without any trace of prepeak (A), also for $q = 0.12 \text{ \AA}^{-1}$, which corresponds to the momentum carried by x-ray photons absorbed at 1.5 KeV energy in the Al K edge XAS. Instead, as the q value further increases, prepeak (A) becomes progressively more visible and intensifies in the loss function. It becomes clearly detectable in the spectrum for $q \gtrsim 4 \text{ \AA}^{-1}$. This behavior demonstrates its nondipolar origin unequivocally.

Besides changing their relative intensities, the three main features (A), (B), and (C) do not show appreciable dispersions as a function of the momentum transfer \mathbf{q} . Only exciton peak (B) slightly disperses (by 0.1 eV) to higher energies for \mathbf{q}

along z . The nondispersive character of these excitations is a manifestation of their localized nature.

In summary, our BSE calculations highlight the strong core excitonic effects at the Al K edge of XAS and XRS. The combination of absorption and loss function spectra strongly supports the nondipolar Al $1s \rightarrow 3s$ character of exciton prepeak (A). It becomes visible in the spectra either for a coupling with atomic vibrations or at finite momentum transfers \mathbf{q} . Our results based on the solution of the many-body BSE agree with the single-particle DFT-based approach [37,38,78,84], where the final state is calculated for a supercell with a core-hole localized on the absorbing atom [85]. The strong electron-hole attraction is explicitly accounted for in the BSE by the screened Coulomb interaction term W , and implicitly in the DFT approach by allowing for electronic relaxation in presence of a core hole [86].

B. Resonant inelastic x-ray scattering at Al L_1 and K edges

While, in principle, unoccupied p states could be equivalently probed in XAS by excitations from either $1s$ or $2s$ core levels, theoretical and experimental investigations have predominantly focused on K edges disregarding L_1 edges. In the independent-particle picture, excitation spectra of α -Al₂O₃ at Al K and L_1 edges can be described by the same unoccupied Al $3p$ PDOS [87]. When excitonic effects are taken into account, instead, one could expect that the higher degree of localization of the $1s$ core hole could lead to stronger electron-hole interactions at the K edge than at the L_1 edge. Their impact on the spectra would therefore be different.

Instead, in the left panel of Fig. 3, the comparison of the Al K and L_1 XAS spectra calculated within the BSE shows that their equivalence also holds beyond the independent-particle picture. Indeed, the two calculated spectra are extremely similar, besides a small shift (<0.1 eV) of the main peak and an overall scaling factor of 35 of the intensity of the L_1 edge with respect to the K edge (the former being more intense than the latter).

Moreover, the right panel of Fig. 3 shows that also RIXS spectra calculated from the BSE at the L_1 and K edges overlap almost entirely for all the incoming photon energy ω_1 spanning a wide energy range of 2.6 eV across the corresponding XAS edge. Therefore, our detailed comparison of both XAS and RIXS spectra suggests that the less common L_1 edge could be equivalently utilized (if the background is not too high) at the place of the K edge. To the best of our knowledge, RIXS spectra of α -Al₂O₃ have not been measured at these edges yet. Our calculations thus represent a prediction for the direct RIXS channel. In the following, we will analyze in detail only the RIXS spectra at the L_1 edge, since the K edge RIXS yields the same information.

Following Shirley and coworkers [21,57,88], we can distinguish two qualitatively different regimes for RIXS spectra (even though this separation is not sharp). For incoming photon energies below the XAS onset (i.e., for $\omega_1 < E_{\lambda_\mu} \forall \lambda_\mu$), the energy conservation in Eq. (9) implies that peaks in the spectra are located at the same energy losses $\omega = \omega_1 - \omega_2 = E_{\lambda_o}$ independently of the excitation energy ω_1 . Equivalently, the emission photon energies $\omega_2 = \omega_1 - E_{\lambda_o}$ increase lin-

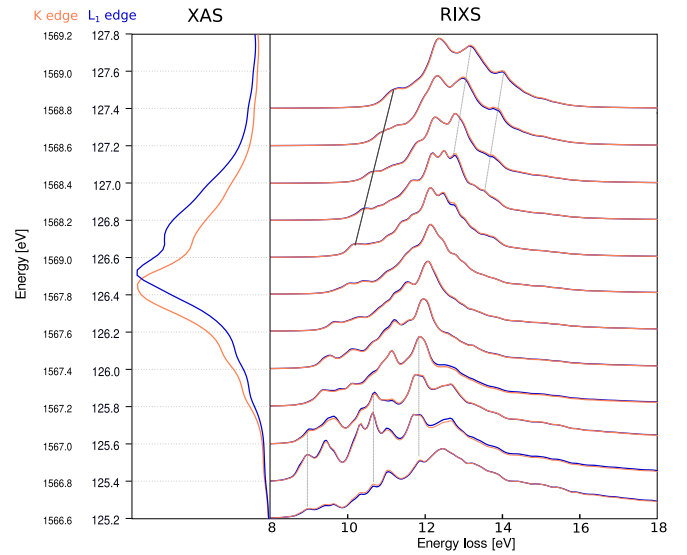


FIG. 3. Left: XAS spectra calculated in the BSE for the Al K and L_1 edges (orange and blue curves, respectively) for polarization along the xy direction. Note the different energy scales for the two edges. The spectrum for the K edge has been multiplied by 35. Both spectra have been convoluted with a 0.1 eV Lorentzian broadening. Right: RIXS spectra at the K and L_1 edges (orange and blue curves, respectively) as a function of the energy loss ω , evaluated for excitation energies ω_1 (separated by 0.2 eV steps) across the corresponding XAS edge in the left panel. The RIXS spectra have been calculated within the BSE for photon polarization vectors \mathbf{e}_1 and \mathbf{e}_2 along the x direction. Each RIXS spectrum has been normalized to its maximum. The thin black lines connecting the different RIXS spectra are guides for the eye to identify Raman losses and fluorescence features.

early with increasing incoming photon energies ω_1 . In this case, the excitations are said to have a *Raman-like* behavior (i.e., nondispersing in an energy-loss representation). Instead, for incoming photon energies ω_1 above the XAS onset, the denominators in Eq. (9) enhance the resonant conditions $\omega_1 = E_{\lambda_\mu}$ (within an energy range dictated by the inverse lifetime Γ). In this regime, the energies of the peaks in the spectra increase linearly with the excitation energies ω_1 . They are thus located at constant emission energies ω_2 , displaying a *fluorescence-like* behavior (i.e., dispersing in an energy-loss representation)

The right panel of Fig. 3 illustrates how the BSE approach is capable of capturing both regimes (the thin black lines across the different spectra indicate these two regimes). Indeed, for excitation energies ω_1 below the edge, we can identify several Raman peaks in the RIXS spectra that are located at constant energy loss, even though their shape strongly changes with ω_1 . Such changes in the spectrum with only small variations in ω_1 cannot be explained in terms of a XAS modulation, highlighting the coherence between the absorption and emission processes. For excitation energies ω_1 above the edge, instead, all the main structures of the RIXS spectra qualitatively change their behavior, displaying a linear dependence on the excitation energy, i.e., they become fluorescences. Due to their different nature, we will analyze these two regimes in more detail, separately.

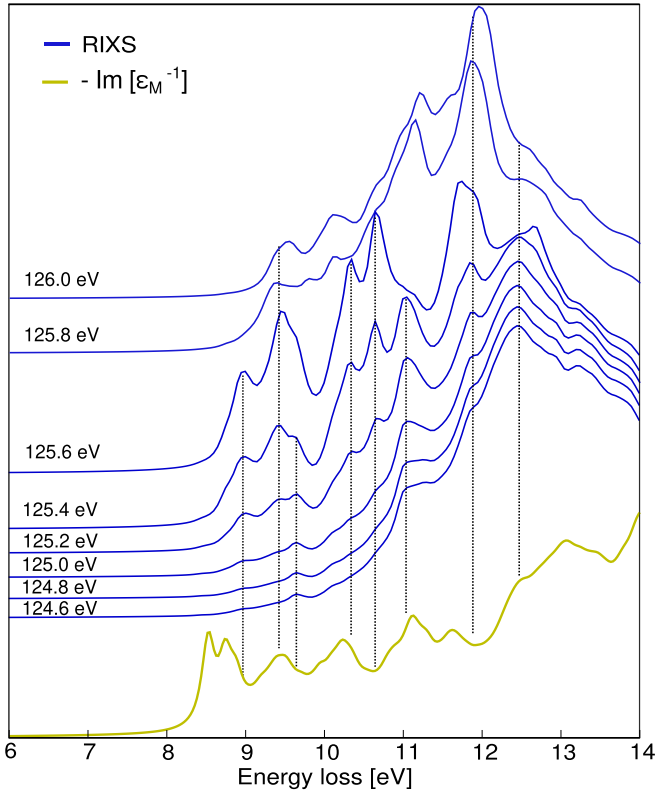


FIG. 4. BSE RIXS spectra (blue curves) as a function of the energy loss ω at the L_1 edge for excitation energies $\omega_1 < 126$ eV. They are compared to the BSE loss function $-\text{Im}\epsilon_M^{-1}(\omega)$ (dark yellow curve) for $\mathbf{q} \rightarrow 0$ along the x direction. The black dotted lines connect Raman peak in RIXS spectra with corresponding inelastic losses in $-\text{Im}\epsilon_M^{-1}(\omega)$. Each spectrum has been normalized to its maximum and offset for clarity.

1. RIXS up to the XAS threshold: Connection with the loss function

Figure 4 focuses on the L_1 RIXS spectra for incoming photon energies ω_1 taken every 0.2 eV between 124.6 and 126 eV, i.e., below the XAS threshold.

The RIXS spectra are also compared to the loss function (8) for $\mathbf{q} \rightarrow 0$. Even though the possible excitation energies E_{λ_0} in RIXS and in the loss function are the same [Eqs. (8)–(9) share the same energy conservation terms], the corresponding peak intensities in the two cases are generally very different [in particular, in the RIXS spectra they are also strongly dependent on the incoming photon energy ω_1 , which enhances features at resonant energies through the denominators in Eq. (9)]. Moreover, since in a solid the possible excitation energies E_{λ_0} form a continuum, matching the corresponding features on the basis of a direct comparison of the spectra is generally not obvious (see the vertical lines in Fig. 4). For the α - Al_2O_3 spectra in Fig. 4, in particular, the most evident discrepancy are the two peaks in the loss function below 9 eV that are missing in the RIXS spectra. They correspond to two bound excitons [59] located inside the band gap of α - Al_2O_3 . We can therefore wonder, Why aren't they also visible in the RIXS spectra? And more in general, how can we use the information from the BSE eigenvalues and eigenfunctions to analyze RIXS spectra and connect them with the loss function?

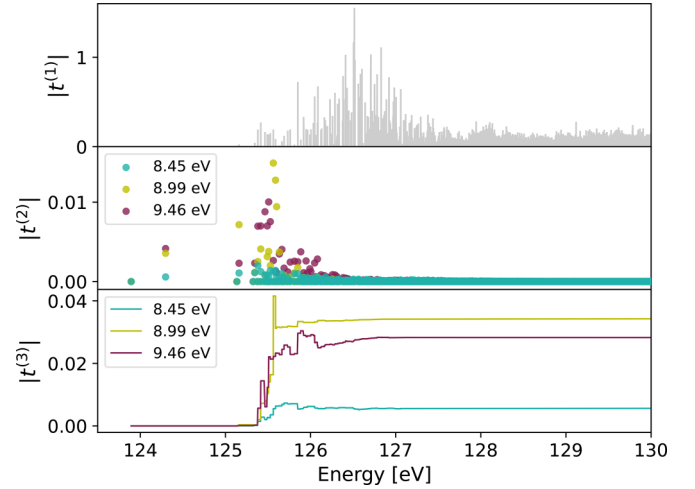


FIG. 5. Absorption oscillator strengths $|t_{\lambda_\mu}^{(1)}|$ (top) and excitation pathways $|t_{\lambda_\mu}^{(2)}|$ (center) as a function of core excitation energy E_{λ_μ} compared to the cumulative RIXS oscillator strengths $|t_{\lambda_0}^{(3)}(E)|$ (bottom) for different exciton energies E_{λ_0} : 8.45, 8.99, and 9.46 eV, as specified in the legends. In the four cases, the incoming photon energy ω_1 is set to 125.6 eV.

To address these questions in detail and analyze the interference between core and valence excitons, we introduce the cumulative oscillator strength $t^{(3)}$ for the peak of energy E_{λ_0} in the RIXS spectrum:

$$t_{\lambda_0}^{(3)}(E) = \sum_{\lambda_\mu}^{E_{\lambda_\mu} < E} \frac{t_{\lambda_\mu}^{(1)} t_{\lambda_0, \lambda_\mu}^{(2)}}{\omega_1 - E_{\lambda_\mu} + i\Gamma/2}. \quad (14)$$

For $E \rightarrow \infty$, $|t_{\lambda_0}^{(3)}|^2$ yields the peak intensity in the RIXS spectrum (calculated for incoming photon energy ω_1) associated to the excitation energy E_{λ_0} . Its plot as a function of the energy E reflects the interference between absorption and emission processes, represented by the terms $t^{(1)}$ and $t^{(2)}$ at the numerator of Eq. (14), respectively. Since they are complex numbers, the interference can be constructive or destructive, displaying the many-body character of the excitations [59,89]. At the same time, the denominator of Eq. (14) also may cross zero for $E_{\lambda_\mu} \sim \omega_1$, expressing the resonant nature of RIXS. As a result, $|t_{\lambda_0}^{(3)}|$ is generally not a monotonic function of the energy E .

The top and middle panels of Fig. 5, respectively, show the absorption oscillator strengths $|t_{\lambda_\mu}^{(1)}|$ [see Eq. (10)], and the excitation pathways $|t_{\lambda_0, \lambda_\mu}^{(2)}|$ for a few selected valence excitons E_{λ_0} (see Eq. (11)), as a function of the core excitation energy E_{λ_μ} . To understand why the first peak in the loss function is not visible in RIXS, in the bottom panel of Fig. 5 we analyze the cumulative oscillator strength $|t_{\lambda_0}^{(3)}(E)|$. In this analysis, the incoming photon energy ω_1 is set to 125.6 eV, corresponding to the highest energy for which Raman features are noticeable. The behavior of the valence exciton with energy $E_{\lambda_0} = 8.45$ eV is compared with those of the excitons at energies $E_{\lambda_0} = 8.99$ eV and 9.46 eV, corresponding to the first two visible peaks in the RIXS spectra. For all the valence excitons E_{λ_0} , the excitation pathways $|t_{\lambda_0, \lambda_\mu}^{(2)}|$ are not zero at low excitation energies $E_{\lambda_\mu} < 125$ eV, where the absorption oscillators $|t_{\lambda_\mu}^{(1)}|$ are instead negligible, due to the

forbidden nature of the transition between the Al $2s$ core level and the bottom of the conduction band, primarily of Al $3s$ character. Accordingly, they do not contribute to the RIXS spectrum. For the exciton $E_{\lambda_o} = 8.45$ eV, the values of the other excitation pathways $|t_{\lambda_o, \lambda_\mu}^{(2)}|$ are very small, canceling out the contributions of the absorption oscillators $|t_{\lambda_\mu}^{(1)}|$ for all other E_{λ_μ} energies. The resulting oscillator strength $|t_{\lambda_o}^{(3)}(E)|$ is therefore always very small and, as a consequence, the exciton is not visible in the RIXS spectrum. For the other valence excitons E_{λ_o} corresponding to the visible peaks in the RIXS spectrum, instead, the emission contributions $|t_{\lambda_o, \lambda_\mu}^{(2)}|$ provide constructive interference with the absorption oscillators $|t_{\lambda_\mu}^{(1)}|$ at higher E_{λ_μ} energies. As a result, the peaks are visible in the RIXS spectrum.

From this analysis, we can therefore conclude that the lowest-energy peaks in the loss function (see the yellow curve in Fig. 4) are not visible in the RIXS spectra because the first absorption step, corresponding to the excitation from core $2s$ level to the bottom conduction states, is forbidden. In the Al L_1 and K edges of α -Al $_2$ O $_3$, RIXS in the direct channel is not able to probe the lowest energy valence exciton states involving combinations of top-valence and bottom-conduction states, but only excitons with higher energies ($\gtrsim 9$ eV) stemming from higher conduction states.

2. RIXS at and beyond the XAS threshold: Excitonic effects fading away and connection with XES

Figure 6 presents BSE and IPA RIXS spectra for excitation energies ω_1 across and above the XAS Al L_1 threshold. The two series of spectra have been obtained from Eqs. (9) and (12), respectively. Note that to highlight fluorescence features, here the spectra have been plotted as a function of the emission photon energy ω_2 , instead of the energy loss ω , as shown in Figs. 3 and 4.

Below the threshold and for energies up to 128.2 eV, large differences between IPA and BSE spectra are noticeable. This implies that strong excitonic effects impact RIXS in α -Al $_2$ O $_3$, making it impossible an interpretation based only on a band-structure picture. One should therefore adopt a many-body picture, where the intermediate and final states correspond to a superposition of many single-particle states at different crystal momenta and from different bands.

On the contrary, for incoming photon energies ω_1 well above the XAS threshold, the IPA and the BSE provide quite similar results. In this regime, the features observed at constant emission energy are indicative of a two-step fluorescence process, where absorption and emission are independent. Consequently, the absorption process [represented by the $t^{(1)}$ contributions in Eq. (9)] acts as a scaling factor and the RIXS spectrum is characterized by fluorescence features [determined by the $t^{(2)}$ contributions in Eq. (9)]. At high incoming photon energies, since excitonic effects are negligible, the BSE RIXS (9) becomes similar to IPA RIXS (12), and since absorption and emission are decoupled, the RIXS spectrum also becomes very close to the XES spectrum (6).

Moreover, as evidenced by Fig. 7, the XES spectrum can be very well described by the angular p component of Al in the PDOS for the valence band. The PDOS shows peaks between

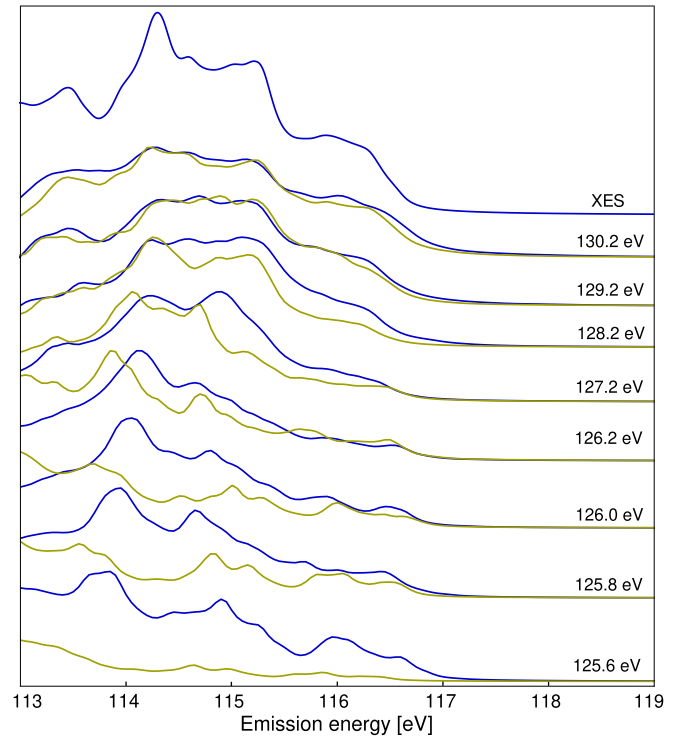


FIG. 6. Comparison between BSE (blue curves) and IPA (dark yellow curve) RIXS spectra as a function of the emission energy ω_2 for different excitation energies ω_1 across the XAS Al L_1 threshold and above it. The fluorescence features are also compared with the XES spectrum (blue curve at the top) at the same Al edge. The RIXS spectrum has been calculated for \mathbf{e}_1 and \mathbf{e}_2 along the x direction, and the XES spectrum for $\mathbf{q} \rightarrow 0$ in the x direction. In the plot, each spectrum has been normalized to its maximum and offset for clarity.

–20 eV and –15 eV, corresponding to aluminum $3p$ states hybridized with the oxygen $2s$ states. Separated by a large gap of ~ 8 eV, starting at ~ -7 eV up to the maximum of

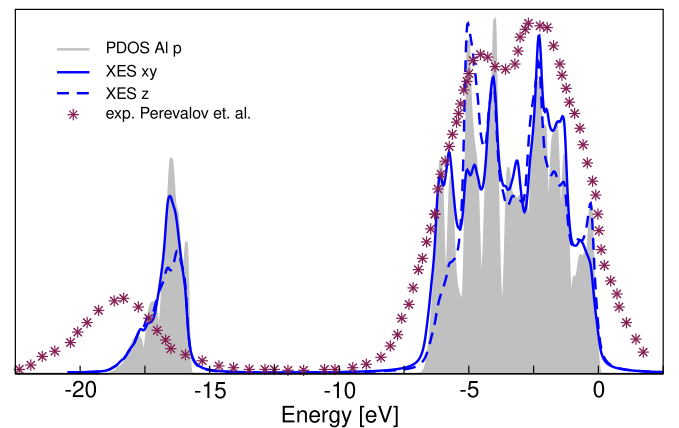


FIG. 7. Comparison between experimental x-ray emission spectrum at Al K edge extracted from Ref. [90] and calculated XES within IPA for the two polarization directions xy and z . The calculated XES can be well described by the Al $3p$ component of the PDOS. In all cases, the top of the valence band in the PDOS and the XES have been set to 0 eV.

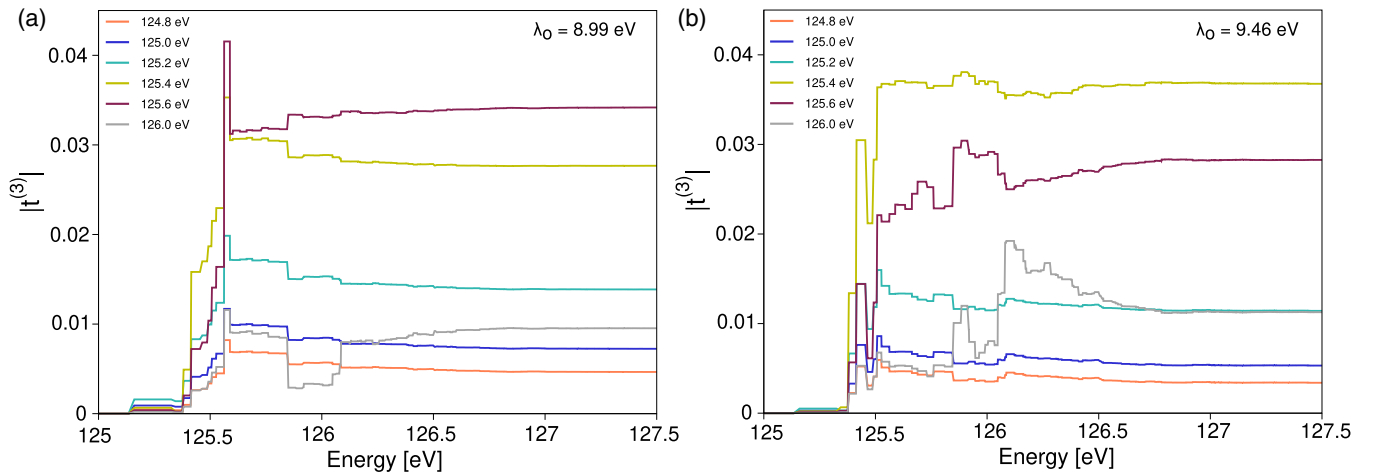


FIG. 8. Cumulative function $|t_{\lambda_o}^{(3)}(E)|$ for different incoming photon energies within the Raman regime. The two panels represent different optical exciton energies E_{λ_o} , associated to RIXS peaks at energy loss of (a) 8.99 eV and (b) 9.46 eV, as seen in Fig. 4.

the valence band set at 0 eV, one finds Al 3*p* states mostly hybridized with O 2*p* states. Even though the separation between the O 2*s* and 2*p* groups of bands is underestimated in the LDA, the calculations reproduce very well the experimental XES spectrum from Ref. [90], including the two-peak structure in the O 2*p* valence band.

Even in a material like α -Al₂O₃, where strong excitonic effects are at play (for both core and valence excitations), we can therefore conclude that at high photon energy ω_1 RIXS is still capable of providing information about band-structure properties.

To understand how Raman features in RIXS spectra give way to fluorescence features as the incoming photon energy ω_1 increases, we examine the dependence of the oscillator strengths $t_{\lambda_o}^{(3)}$ (14) on ω_1 , for specific optical excitons $E_{\lambda_o} = 8.99$ eV and 9.46 eV, as shown in Fig. 8. The two plots show that for incoming photon energies below the XAS threshold (125.6 eV), the interference patterns are relatively constant. On the other hand, the intensity increases accordingly with the resonance between ω_1 and the core exciton energies E_{λ_μ} ,

reaching the highest value at $\omega_1 = 125.4$ –126.6 eV. Beyond this energy, the oscillator strength decays as a result of two effects: the loss of resonance (for the two specific optical excitons λ_o considered here) and the change in the interference pattern produced by the sign in the denominator of Eq. (9). As a result, $|t_{\lambda_o}^{(3)}(E)|$ becomes negligible in the case of the first peak, at an energy loss of 8.99 eV, while it remains visible but with lower intensity at 9.46 eV. This explains the RIXS features of Fig. 4, where the first peak disappears after $\omega_1 = 125.6$ eV and the second peak is visible up to $\omega_1 = 126.0$ eV.

The second observation that can be extracted from the plots is that even though the absorption oscillator strength $t_{\lambda_\mu}^{(1)}$ and excitation pathways $t_{\lambda_o, \lambda_\mu}^{(2)}$ are the same for a given λ_o , when the incoming photon energies are beyond the XAS threshold, the contributions to $|t_{\lambda_o}^{(3)}|$ tend to shift to higher energies as ω_1 increases. This trend is more noticeable in the fluorescence regime, which will be explained below.

Figure 9 shows the absolute value of the absorption oscillator strengths $|t_{\lambda_\mu}^{(1)}|$ and the excitation pathways $|t_{\lambda_o, \lambda_\mu}^{(2)}|$ for (left)

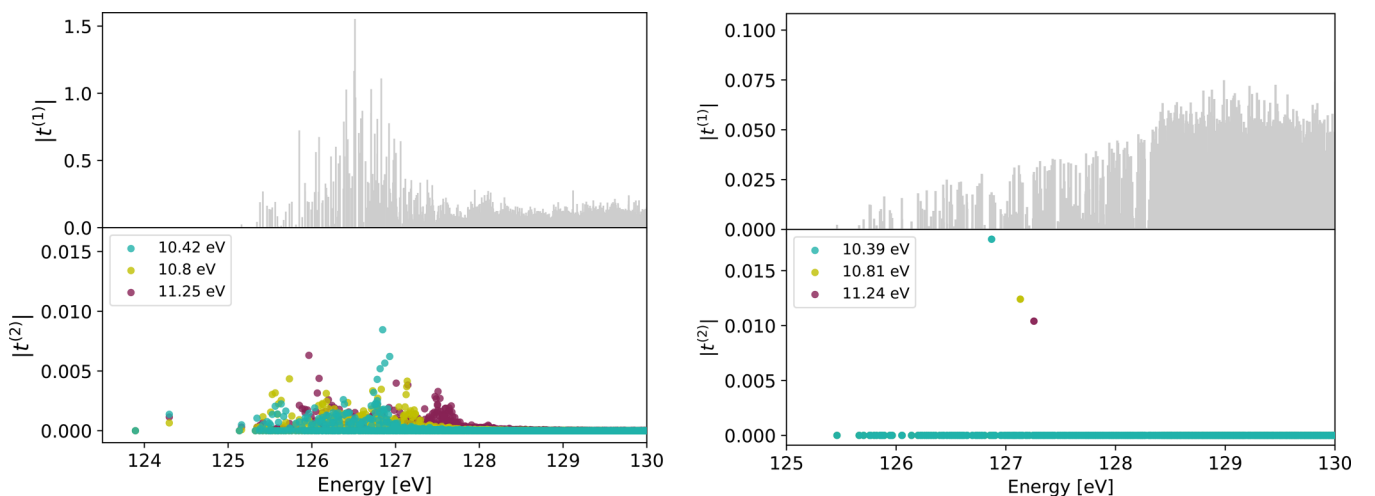


FIG. 9. Absolute value of the absorption oscillator strength $|t_{\lambda_\mu}^{(1)}|$ and the excitation pathways $|t_{\lambda_o, \lambda_\mu}^{(2)}|$ as a function of the core excitation energy E_{λ_μ} for valence excitations $E_{\lambda_o} = 10.4$ eV, 10.8 eV and 11.2 eV, as specified in the legends, for (left) BSE and (right) IPA RIXS.

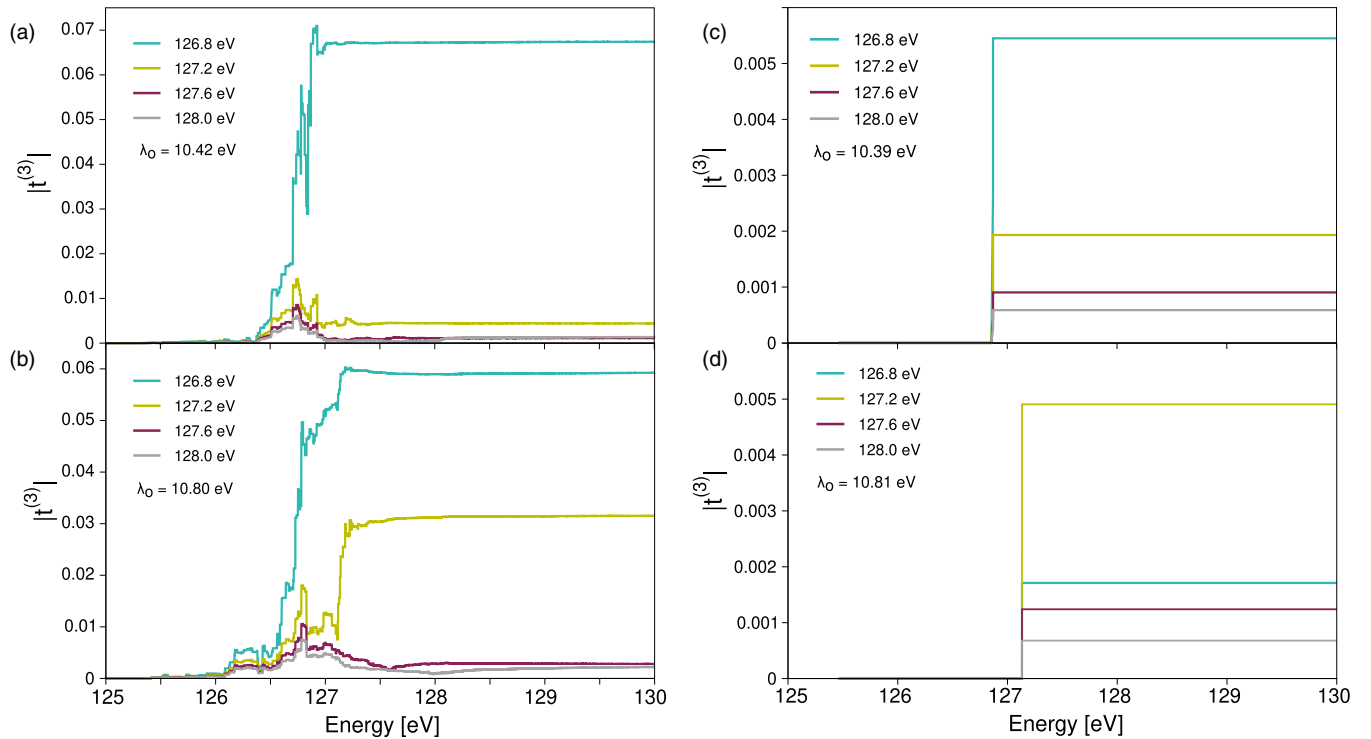


FIG. 10. Cumulative function $|t_{\lambda_o}^{(3)}(E)|$ for different incoming photon energies ω_1 in the fluorescence regime obtained with the BSE for optical excitation energies E_{λ_o} of (a) 10.42 eV and (b) 10.80 eV. Similarly, in the right panels the $|t_{\lambda_o}^{(3)}(E)|$ has been plotted, calculated within IPA for E_{λ_o} equal to (c) 10.39 eV and (d) 10.81 eV.

BSE and (right) IPA RIXS, at three different energy losses: 10.4, 10.8, and 11.2 eV. The resulting cumulative oscillator strengths $|t_{\lambda_o}^{(3)}|$ are shown in Fig. 10 for BSE RIXS at two E_{λ_o} values: (a) 10.42 eV and (b) 10.80 eV. Similarly, the $|t_{\lambda_o}^{(3)}|$ calculated within IPA are displayed in Figs. 10(c) for $\lambda_o = 10.39$ eV and 10(d) for $\lambda_o = 10.81$ eV. Figures 9 and 10 highlight the fact that, given a specific optical exciton λ_o , the differences in the $|t_{\lambda_o}^{(3)}|$ with incoming photon energy ω_1 are only given by the effect of the denominator of Eq. (9), as discussed above.

Here, it is interesting to note that the largest contributions of the excitation pathways $|t_{\lambda_o, \lambda_\mu}^{(2)}|$ in Fig. 9 tend to be centered around higher core excitation energies E_{λ_μ} as the energy of the valence excitons E_{λ_o} increases (this has been also observed in Fig. 5). These excitons stem from electron-hole transitions of higher energies, originating from valence and conduction states farther away from the top valence and bottom conduction, respectively. Correspondingly, a larger excitation energy E_{λ_μ} is required to probe those higher-energy conduction states.

If one compares the RIXS oscillator strengths in Fig. 10 for the BSE [Figs. 10(a) and 10(b)] and IPA [Figs. 10(c) and 10(d)], it is possible to conclude that the blueshifts in the energy contributions to $|t_{\lambda_o}^{(3)}|$ for increasing ω_1 are the result of the excitonic effects, which give more weight to higher core excitons as ω_1 increases, while in the IPA picture the jump in $|t_{\lambda_o}^{(3)}|$ is given at a constant energy E_{λ_μ} for all ω_1 .

If we compare the four panels in Fig. 10, it is noticeable how only low ω_1 (126.8 eV) lead to non-negligible RIXS oscillator strengths $|t_{\lambda_o}^{(3)}|$ at low energy-loss peaks E_{λ_o}

[Figs. 10(a) and 10(c)]. If the incoming energy is increased, they become more prominent as the energy loss increases [Figs. 10(b) and 10(d)]. This analysis provides the last piece to understand the movement of peaks in the fluorescence regime. The fact that the excitation pathways $|t_{\lambda_o, \lambda_\mu}^{(2)}|$ shift to higher core energies E_{λ_μ} as one moves to higher optical excitation energies E_{λ_o} (or energy loss) imposes resonance [according to Eq. (9)] at higher incoming photon energy ω_1 . Consequently, the increase of ω_1 causes the RIXS oscillator strength $|t_{\lambda_o}^{(3)}|$ to become more intense at higher E_{λ_o} .

As a summary, one can highlight that within the many-body picture, ω_1 has two main effects: (1) before the XAS edge, it acts as a scaling factor, leaving the role of the interference to the interplay between $t^{(1)}$ and $t^{(2)}$ at each optical exciton energy E_{λ_o} ; and (2) for incoming photon energies in resonance and beyond the XAS edge, it determines for each core exciton λ_μ whether the interference between $t_{\lambda_\mu}^{(1)}$ and $t_{\lambda_o, \lambda_\mu}^{(2)}$ will be constructive or destructive according to the sign.

IV. CONCLUSIONS

We have presented an in-depth analysis of RIXS spectra, considering coherence and excitonic effects throughout the process. Additionally, we have established several connections between RIXS and complementary spectroscopy techniques that assess neutral excitations in materials, specifically XAS, XRS, and XES. We have applied the BSE approach to study core and semicore excitations of corundum $\alpha\text{-Al}_2\text{O}_3$, a widely used material due to its optical and structural properties.

The comparison between experimental Al K edge XAS spectra and calculated spectra at different polarization directions has demonstrated that excitonic effects are crucial to reproduce most features of the experimental data. The experimental prepeak (A) observed at ~ 1566 eV is a dark exciton representing dipole-forbidden transitions in the calculations. However, it becomes a bright exciton in the calculated loss functions at finite momentum transfers, which includes multipole contributions.

Remarkably, our paper reveals that both XAS and RIXS spectra, even when calculated within the BSE, at the K and L_1 edges exhibit a high degree of agreement. This result suggests the use of soft x-ray techniques for studying the L_1 edge and extracting the same information as the traditionally explored K edge.

For excitation energies below the XAS onset, the RIXS spectra show a Raman-like behavior, where the energy losses remain constant as the incident photon energy ω_1 is varied. The comparative analysis of the Raman losses between RIXS and the loss function sheds light on differences in selection rules and intensity enhancements between the two techniques. Beyond the XAS threshold, RIXS displays a two-step fluorescence behavior, with peaks shifting in accordance with ω_1 ,

highlighting the loss of coherence between the absorption and the emission processes. The agreement with XES emphasizes the similarities between fluorescence and emission. In the same fashion, excitonic effects become weaker for excitation energies ω_1 well above the threshold. Therefore, if one wishes to probe valence excitons by RIXS, excitation energies ω_1 below or at the edge should be selected. Conversely, if band-structure properties are the target, higher excitation energies ω_1 should be preferred.

Altogether, these findings contribute to a deeper understanding of the RIXS process, its behavior in different energy regimes, and its connection with other spectroscopic techniques, facilitating further insights into materials' electronic properties.

ACKNOWLEDGMENTS

We acknowledge valuable discussions with C. Vorwerk and thank D. Cabaret for kindly sharing data with us from Refs. [37,38]. We acknowledge the French Agence Nationale de la Recherche (ANR) for financial support (Grant Agreement No. ANR-19-CE30-0011). Computational time was granted by GENCI (Project No. 544).

-
- [1] P. Zimmermann, S. Peredkov, P. M. Abdala, S. De Beer, M. Tromp, C. Müller, and J. A. van Bokhoven, *Modern X-ray spectroscopy: XAS and XES in the laboratory*, *Coord. Chem. Rev.* **423**, 213466 (2020).
- [2] L. J. P. Ament, M. van Veenendaal, T. P. Devereaux, J. P. Hill, and J. van den Brink, Resonant inelastic X-ray scattering studies of elementary excitations, *Rev. Mod. Phys.* **83**, 705 (2011).
- [3] F. de Groot, High-resolution X-ray emission and X-ray absorption spectroscopy, *Chem. Rev.* **101**, 1779 (2001).
- [4] J. J. Rehr and R. C. Albers, Theoretical approaches to X-ray absorption fine structure, *Rev. Mod. Phys.* **72**, 621 (2000).
- [5] J. J. Rehr, Theory and calculations of X-ray spectra: XAS, XES, XRS, and NRIXS, *Radiat. Phys. Chem.* **75**, 1547 (2006).
- [6] F. M. F. de Groot, H. Elnaggar, F. Frati, R.-pan. Wang, M. U. Delgado-Jaime, M. van Veenendaal, J. Fernandez-Rodriguez, M. W. Haverkort, R. J. Green, G. van der Laan, Y. Kvashnin, A. Hariki, H. Ikeno, H. Ramanantoanina, C. Daul, B. Delley, M. Odellius, M. Lundberg, O. Kuhn, S. I. Bokarev *et al.*, 2p X-ray absorption spectroscopy of 3D transition metal systems, *J. Electron Spectrosc. Relat. Phenom.* **249**, 147061 (2021).
- [7] F. De Groot and A. Kotani, *Core Level Spectroscopy of Solids* (CRC Press, Boca Raton, Florida, 2008).
- [8] J. A. van Bokhoven and C. Lamberti, *X-Ray Absorption and X-Ray Emission Spectroscopy: Theory and Applications* (Wiley, Hoboken, New Jersey, 2016), Vol. 1.
- [9] S. Huotari, Spectroscopy in the frequency domain, in *Fundamentals of Time-Dependent Density Functional Theory*, edited by Miguel A. L. Marques, N. T. Maitra, F. M. S. Nogueira, E. K. U. Gross, and A. Rubio (Springer, Berlin, 2012), pp. 15–28.
- [10] W. Schülke, *Electron Dynamics by Inelastic X-Ray Scattering*, Oxford Series on Synchrotron Radiation (Oxford University Press, Oxford, 2007).
- [11] A. Kotani and S. Shin, Resonant inelastic X-ray scattering spectra for electrons in solids, *Rev. Mod. Phys.* **73**, 203 (2001).
- [12] U. von Barth and G. Grossmann, Dynamical effects in X-ray spectra and the final-state rule, *Phys. Rev. B* **25**, 5150 (1982).
- [13] J. J. Rehr, J. A. Soininen, and E. L. Shirley, Final-state rule vs the Bethe-Salpeter equation for deep-core X-ray absorption spectra, *Phys. Scr.* **2005**, 207 (2005).
- [14] S. I. Zabinsky, J. J. Rehr, A. Ankudinov, R. C. Albers, and M. J. Eller, Multiple-scattering calculations of X-ray-absorption spectra, *Phys. Rev. B* **52**, 2995 (1995).
- [15] J. A. Soininen, A. L. Ankudinov, and J. J. Rehr, Inelastic scattering from core electrons: A multiple scattering approach, *Phys. Rev. B* **72**, 045136 (2005).
- [16] J. J. Kas, J. J. Rehr, J. A. Soininen, and P. Glatzel, Real-space Green's function approach to resonant inelastic X-ray scattering, *Phys. Rev. B* **83**, 235114 (2011).
- [17] I. Josefsson, K. Kunnus, S. Schreck, A. Föhlisch, F. de Groot, P. Wernet, and M. Odellius, Ab initio calculations of X-ray spectra: Atomic multiplet and molecular orbital effects in a multiconfigurational SCF approach to the L-edge spectra of transition metal complexes, *J. Phys. Chem. Lett.* **3**, 3565 (2012).
- [18] M. W. Haverkort, M. Zwierzycki, and O. K. Andersen, Multiplet ligand-field theory using Wannier orbitals, *Phys. Rev. B* **85**, 165113 (2012).
- [19] D. Maganas, P. Kristiansen, L.-C. Duda, A. Knop-Gericke, S. DeBeer, R. Schlögl, and F. Neese, Combined experimental and ab initio multireference configuration interaction study of the resonant inelastic X-ray scattering spectrum of Co_2 , *J. Phys. Chem. C* **118**, 20163 (2014).
- [20] E. L. Shirley, Ab initio inclusion of electron-hole attraction: Application to X-ray absorption and resonant inelastic X-ray scattering, *Phys. Rev. Lett.* **80**, 794 (1998).
- [21] E. L. Shirley, Theory and simulation of resonant inelastic X-ray scattering in s - p bonded systems: Graphite, hexagonal boron

- nitride, diamond, and cubic boron nitride, *J. Electron Spectrosc. Relat. Phenom.* **110-111**, 305 (2000).
- [22] E. L. Shirley, J. A. Soininen, G. P. Zhang, J. A. Carlisle, T. A. Callcott, D. L. Ederer, L. J. Terminello, and R. C. C. Perera, Modeling final-state interaction effects in inelastic X-ray scattering from solids: Resonant and non-resonant, *J. Electron Spectrosc. Relat. Phenom.* **114-116**, 939 (2001).
- [23] J. Vinson, J. J. Rehr, J. J. Kas, and E. L. Shirley, Bethe-Salpeter equation calculations of core excitation spectra, *Phys. Rev. B* **83**, 115106 (2011).
- [24] J. Vinson, T. Jach, M. Müller, R. Unterumsberger, and B. Beckhoff, Quasiparticle lifetime broadening in resonant X-ray scattering of NH_4NO_3 , *Phys. Rev. B* **94**, 035163 (2016).
- [25] J. Vinson, T. Jach, M. Müller, R. Unterumsberger, and B. Beckhoff, Resonant X-ray emission of hexagonal boron nitride, *Phys. Rev. B* **96**, 205116 (2017).
- [26] J. Vinson, T. Jach, M. Müller, R. Unterumsberger, and B. Beckhoff, Resonant X-ray emission and valence-band lifetime broadening in LiNO_3 , *Phys. Rev. B* **100**, 085143 (2019).
- [27] C. Vorwerk, F. Sottile, and C. Draxl, Excitation pathways in resonant inelastic X-ray scattering of solids, *Phys. Rev. Res.* **2**, 042003(R) (2020).
- [28] C. Vorwerk, F. Sottile, and C. Draxl, All-electron many-body approach to resonant inelastic X-ray scattering, *Phys. Chem. Chem. Phys.* **24**, 17439 (2022).
- [29] K. Gilmore, J. Pellicciari, Y. Huang, J. J. Kas, M. Dantz, V. N. Strocov, S. Kasahara, Y. Matsuda, T. Das, T. Shibauchi, and T. Schmitt, Description of resonant inelastic X-ray scattering in correlated metals, *Phys. Rev. X* **11**, 031013 (2021).
- [30] G. Strinati, Application of the Green's functions method to the study of the optical properties of semiconductors, *Riv. Nuovo Cimento (1978-1999)* **11**, 1 (1988).
- [31] W. Hanke and L. J. Sham, Many-particle effects in the optical excitations of a semiconductor, *Phys. Rev. Lett.* **43**, 387 (1979).
- [32] F. Bechstedt, *Many-Body Approach to Electronic Excitations: Concepts and Applications*, Springer Series in Solid-State Sciences (Springer, Berlin, 2014).
- [33] R. M. Martin, L. Reining, and D. M. Ceperley, *Interacting Electrons: Theory and Computational Approaches* (Cambridge University Press, Cambridge, England, 2016).
- [34] C. Vorwerk, B. Aurich, C. Cocchi, and C. Draxl, Bethe-Salpeter equation for absorption and scattering spectroscopy: Implementation in the exciting code, *Electron. Struct.* **1**, 037001 (2019).
- [35] B. Lin, L. Heng, B. Fang, H. Yin, J. Ni, X. Wang, J. Lin, and L. Jiang, Ammonia synthesis activity of alumina-supported ruthenium catalyst enhanced by alumina phase transformation, *ACS Catal.* **9**, 1635 (2019).
- [36] T. W. Hickmott, Low-frequency negative resistance in thin anodic oxide films, *J. Appl. Phys.* **33**, 2669 (1962).
- [37] D. Manuel, D. Cabaret, C. Brouder, P. Sainctavit, A. Bordage, and N. Trcera, Experimental evidence of thermal fluctuations on the X-ray absorption near-edge structure at the aluminum k edge, *Phys. Rev. B* **85**, 224108 (2012).
- [38] S. Delhommaye, G. Radtke, C. Brouder, S. P. Collins, S. Huotari, C. Sahle, M. Lazzeri, L. Paulatto, and D. Cabaret, Assessing temperature effects on multipole contributions and angular dependence in core-level spectroscopies, *Phys. Rev. B* **104**, 024302 (2021).
- [39] L. Hedin, New method for calculating the one-particle Green's function with application to the electron-gas problem, *Phys. Rev.* **139**, A796 (1965).
- [40] G. Onida, L. Reining, and A. Rubio, Electronic excitations: Density-functional versus many-body Green's-function approaches, *Rev. Mod. Phys.* **74**, 601 (2002).
- [41] For simplicity, here we consider explicitly only a spin-unpolarized situation.
- [42] W. Kohn and L. J. Sham, Self-consistent equations including exchange and correlation effects, *Phys. Rev.* **140**, A1133 (1965).
- [43] N. Wiser, Dielectric constant with local field effects included, *Phys. Rev.* **129**, 62 (1963).
- [44] S. L. Adler, Quantum theory of the dielectric constant in real solids, *Phys. Rev.* **126**, 413 (1962).
- [45] J. C. Taylor, Tamm-Dancoff method, *Phys. Rev.* **95**, 1313 (1954).
- [46] D. R. Mortensen, G. T. Seidler, J. J. Kas, N. Govind, C. P. Schwartz, S. Pemmaraju, and D. G. Prendergast, Benchmark results and theoretical treatments for valence-to-core X-ray emission spectroscopy in transition metal compounds, *Phys. Rev. B* **96**, 125136 (2017).
- [47] T. Aoki and K. Ohno, Ab initio simulations of X-ray emission spectroscopy with the GW +Bethe-Salpeter equation method, *Phys. Rev. B* **100**, 075149 (2019).
- [48] M. Gatti and F. Sottile, Exciton dispersion from first principles, *Phys. Rev. B* **88**, 155113 (2013).
- [49] F. Sottile, F. Bruneval, A. G. Marinopoulos, L. K. Dash, S. Botti, V. Olevano, N. Vast, A. Rubio, and L. Reining, TDDFT from molecules to solids: The role of long-range interactions, *Int. J. Quantum Chem.* **102**, 684 (2005).
- [50] Y. Mizuno and Y. Ohmura, Theory of X-ray raman scattering, *J. Phys. Soc. Jpn.* **22**, 445 (1967).
- [51] Here we consider only the so-called direct RIXS, in contrast to indirect RIXS, where the core hole potential induces secondary excitations [2]. Moreover, we focus on the electronic excitations only.
- [52] Differently from Eq. (4) that adopts a longitudinal gauge, in Eqs. (10) and (11), the oscillator strengths are written in the transverse gauge. The two gauges are equivalent in the long-wavelength limit [91], where the polarization unity vectors \mathbf{e} and the wave vectors \mathbf{q} play the same role, defining the direction of the perturbation. Therefore, the oscillator strengths $t_{\lambda\mu}^{(1)}$ in Eq. (10) are equivalent to those in the XAS spectra from Eq. (3). Similarly, the oscillator strengths $\langle \mu\mathbf{k} | \mathbf{e}_2^* \cdot \mathbf{p} | \nu\mathbf{k} \rangle$ in Eq. (11) correspond to those entering XES spectra in Eq. (6).
- [53] J.-P. Rueff and A. Shukla, Inelastic X-ray scattering by electronic excitations under high pressure, *Rev. Mod. Phys.* **82**, 847 (2010).
- [54] P. D. Johnson and Y. Ma, Band structure and X-ray resonant inelastic scattering, *Phys. Rev. B* **49**, 5024 (1994).
- [55] Y. Ma, X-ray absorption, emission, and resonant inelastic scattering in solids, *Phys. Rev. B* **49**, 5799 (1994).
- [56] J. A. Carlisle, E. L. Shirley, E. A. Hudson, L. J. Terminello, T. A. Callcott, J. J. Jia, D. L. Ederer, R. C. C. Perera, and F. J. Himpsel, Probing the graphite band structure with resonant soft-X-ray fluorescence, *Phys. Rev. Lett.* **74**, 1234 (1995).
- [57] J. A. Carlisle, E. L. Shirley, L. J. Terminello, J. J. Jia, T. A. Callcott, D. L. Ederer, R. C. C. Perera, and F. J. Himpsel,

- Band-structure and core-hole effects in resonant inelastic soft-X-ray scattering: Experiment and theory, *Phys. Rev. B* **59**, 7433 (1999).
- [58] J. A. Carlisle, S. R. Blankenship, L. J. Terminello, J. J. Jia, T. A. Callcott, D. L. Ederer, R. C. C. Perera, and F. J. Himpsel, Crystal-momentum-resolved electronic structure of solids using resonant soft-X-ray fluorescence spectroscopy, *J. Electron Spectrosc. Relat. Phenom.* **110-111**, 323 (2000).
- [59] M. L. Urquiza, M. Gatti, and F. Sottile, Pseudopotential Bethe-Salpeter calculations for shallow-core X-ray absorption near-edge structures: Excitonic effects in α -Al₂O₃, *Phys. Rev. B* **107**, 205148 (2023).
- [60] E. E. Newnham and Y. M. Haan, Refinement of the α -Al₂O₃, Ti₂O₃, V₂O₃ and Cr₂O₃ structures, *Z. Kristallogr. Cryst. Mater.* **117**, 235 (1962).
- [61] A. Gulans, S. Kontur, C. Meisenbichler, D. Nabok, P. Pavone, S. Rigamonti, S. Sagmeister, U. Werner, and C. Draxl, EXCITING: A full-potential all-electron package implementing density-functional theory and many-body perturbation theory, *J. Phys.: Condens. Matter* **26**, 363202 (2014).
- [62] A. G. Marinopoulos and M. Grüning, Local-field and excitonic effects in the optical response of α -alumina, *Phys. Rev. B* **83**, 195129 (2011).
- [63] *Unoccupied Electronic States, Fundamentals for XANES, EELS, IPS and BIS*, edited by J. C. Fuggle and J. E. Inglesfield (Springer Berlin, 2005), p. 347.
- [64] J. L. Campbell and T. Papp, Widths of the atomic K-N7 levels, *At. Data Nucl. Data Tables* **77**, 1 (2001).
- [65] C. W. Vorwerk, Ph.D. thesis, Humboldt-Universität zu Berlin, 2021.
- [66] F. G. Will, H. G. De Lorenzi, and K. H. Janora, Conduction mechanism of single-crystal alumina, *J. Am. Ceram. Soc.* **75**, 295 (1992).
- [67] R. H. French, D. J. Jones, and S. Loughin, Interband electronic structure of α -alumina up to 2167 K, *J. Am. Ceram. Soc.* **77**, 412 (1994).
- [68] A. K. Harman, S. Ninomiya, and S. Adachi, Optical constants of sapphire (α -Al₂O₃) single crystals, *J. Appl. Phys.* **76**, 8032 (1994).
- [69] M. Schubert, T. E. Tiwald, and C. M. Herzinger, Infrared dielectric anisotropy and phonon modes of sapphire, *Phys. Rev. B* **61**, 8187 (2000).
- [70] Y. Kato, K.-I. Shimizu, N. Matsushita, T. Yoshida, H. Yoshida, A. Satsuma, and T. Hattori, Quantification of aluminium coordinations in alumina and silica-alumina by Al K-edge XANES, *Phys. Chem. Chem. Phys.* **3**, 1925 (2001).
- [71] M. Mogi, T. Yamamoto, T. Mizoguchi, K. Tatsumi, S. Yoshioka, S. Kameyama, I. Tanaka, and H. Adachi, Theoretical investigation of Al k-edge X-ray absorption spectra of Al, AlN and Al₂O₃, *Metall. Mater.* **45**, 2031 (2004).
- [72] D. Li, G. M. Bancroft, M. E. Fleet, X. H. Feng, and Y. Pan, Al K-edge XANES spectra of aluminosilicate minerals, *Am. Mineral.* **80**, 432 (1995).
- [73] D. Cabaret, P. Sainctavit, P. Ildefonse, and A.-M. Flank, Full multiple-scattering calculations on silicates and oxides at the Al K edge, *J. Phys.: Condens. Matter* **8**, 3691 (1996).
- [74] P. Ildefonse, D. Cabaret, P. Sainctavit, G. Calas, A.-M. Flank, and P. Lagarde, Aluminium X-ray absorption near edge structure in model compounds and earth's surface minerals, *Phys. Chem. Miner.* **25**, 112 (1998).
- [75] S.-D. Mo and W. Y. Ching, Ab initio calculation of the core-hole effect in the electron energy-loss near-edge structure, *Phys. Rev. B* **62**, 7901 (2000).
- [76] D. Cabaret, E. Gaudry, M. Taillefumier, P. Sainctavit, and F. Mauri, Xanes calculation with an efficient “non muffin-tin” method: Application to the angular dependence of the Al K-edge in corundum, *Phys. Scr.* **2005**, 131 (2005).
- [77] D. Cabaret and C. Brouder, Origin of the pre-edge structure at the Al k-edge: The role of atomic vibrations, *J. Phys.: Conf. Ser.* **190**, 012003 (2009).
- [78] C. Brouder, D. Cabaret, A. Juhin, and P. Sainctavit, Effect of atomic vibrations on the X-ray absorption spectra at the k edge of Al in α -Al₂O₃ and of Ti in TiO₂ rutile, *Phys. Rev. B* **81**, 115125 (2010).
- [79] R. Nemausat, C. Brouder, C. Gervais, and D. Cabaret, First-principles study of phonon effects in X-ray absorption near-edge structure spectroscopy, *J. Phys.: Conf. Ser.* **712**, 012006 (2016).
- [80] P. Cudazzo, First-principles description of the exciton-phonon interaction: A cumulant approach, *Phys. Rev. B* **102**, 045136 (2020).
- [81] H.-Y. Chen, D. Sangalli, and M. Bernardi, Exciton-phonon interaction and relaxation times from first principles, *Phys. Rev. Lett.* **125**, 107401 (2020).
- [82] G. Antonius and S. G. Louie, Theory of exciton-phonon coupling, *Phys. Rev. B* **105**, 085111 (2022).
- [83] P. Cudazzo, Dynamical effects on photoluminescence spectra from first principles: A many-body Green's function approach, *Phys. Rev. B* **108**, 165101 (2023).
- [84] G. B. Grad, E. R. González, J. Torres-Díaz, and E. V. Bonzi, A DFT study of ZnO, Al₂O₃ and SiO₂: Combining X-ray spectroscopy, chemical bonding and Wannier functions, *J. Phys. Chem. Solids* **168**, 110788 (2022).
- [85] Or, also, by using the Z + 1 scheme [92].
- [86] Y. Liang, J. Vinson, S. Pemmaraju, W. S. Drisdell, E. L. Shirley, and D. Prendergast, Accurate X-ray spectral predictions: An advanced self-consistent-field approach inspired by many-body perturbation theory, *Phys. Rev. Lett.* **118**, 096402 (2017).
- [87] S. Nufer, T. Gemming, C. Elsässer, S. Köstlmeier, and M. Rühle, Core-hole effect in the E₁ of α -Al₂O₃: Experiment and theory, *Ultramicroscopy* **86**, 339 (2001).
- [88] J. J. Jia, T. A. Callcott, E. L. Shirley, J. A. Carlisle, L. J. Terminello, A. Asfaw, D. L. Ederer, F. J. Himpsel, and R. C. C. Perera, Resonant inelastic X-ray scattering in hexagonal boron nitride observed by soft-X-ray fluorescence spectroscopy, *Phys. Rev. Lett.* **76**, 4054 (1996).
- [89] A. Lorin, M. Gatti, L. Reining, and F. Sottile, First-principles study of excitons in optical spectra of silver chloride, *Phys. Rev. B* **104**, 235149 (2021).
- [90] T. V. Perevalov, V. A. Gritsenko, and V. V. Kaichev, Electronic structure of aluminum oxide: Ab initio simulations of ses and comparison with experiment for amorphous films, *Eur. Phys. J. Appl. Phys.* **52**, 30501 (2010).
- [91] R. Del Sole and R. Girlanda, Optical properties of semiconductors within the independent-quasiparticle approximation, *Phys. Rev. B* **48**, 11789 (1993).
- [92] K. Nakanishi and T. Ohta, Verification of the FEFF simulations to K-edge XANES spectra of the third row elements, *J. Phys.: Condens. Matter* **21**, 104214 (2009).